Torque-Dense Photomechanical Actuation

Mahnoush Babaei ¹, Junfeng Gao², Arul Clement², Kaushik Dayal ¹ and M. Ravi Shankar^{2*}

¹ Department of Civil and Environmental Engineering and Department of Materials Science and Engineering

Carnegie Mellon University, Pittsburgh, PA

² Department of Industrial Engineering

University of Pittsburgh, Pittsburgh PA

Keywords: Photomechanics, Liquid Crystal Elastomers, Mechanical Instability, Soft Actuators

Abstract

Contactless actuation powered using light is shown to generate torque densities approaching 10

N.m/kg at angular velocities ~10² rad/s: metrics that compare favorably against tethered

electromechanical systems. This is possible even though the extinction of actinic light limits the

characteristic thickness of photoresponse in polymers to tens of um. Confinement of molecularly

patterned developable shells fabricated from azobenzene-functionalized liquid crystalline

polymers encodes torque-dense photoactuation. Photostrain gradients from unstructured

irradiation segment this geometry into two oppositely curved regions connected by a curved

crease. A monolithic curved shell spontaneously bifurcates into a jointed, arm-like mechanism that

generates flexure over sweep angles exceeding a radian. Strain focusing at the crease is

hierarchical: an integral crease nucleates at smaller magnitudes of the prebiased curvature, while

a crease decorated with point-like defects emerges at larger curvatures. The phase-space of

morphogenesis is traceable to the competition between stretch and bending energies and is

parameterizable as a function of the geometry. The framework for generating repetitive torque-

dense actuation from slender light-powered actuators holds broader implications for the design of

soft, remotely operated machines. Here, it is harnessed in illustrative mechanisms including levers,

lifters and grabbers that are powered and regulated exclusively using light.

* ravishm@pitt.edu

1

1. Introduction

Using light to power and control mechanical actuators, whose response profiles compare favorably against conventional actuation systems can enable a new class of "photomechanical machines". Fabricated from otherwise passive materials and not requiring onboard power, it is possible to envision machines that are remotely operated using either directed energy sources or by harvesting photons from the ambient (1-7). Light driven molecular switching via isomerization, that is transduced into mechanical distortion within ordered macromolecular networks (for e.g. liquid crystalline polymers: LCP) is a useful material motif (8). The kinetics of photoisomerization dictates the conformation of the network, which determines the photomechanical distortion (9). Since, nematic order directs the principal strains, voxelated patterning of molecular director is useful for encoding actuation and shape-selection (10-14). Previous efforts have shown promising results for photomechanical manipulation and motility using LCPs (13, 15, 16). Scaling up the actuation profiles is key to translating them into practical applications. Compared to conventional actuators, there is a fundamental constraint on scaling up the photomechanical work-potential: absorption of the light to drive the actuation also attenuates it through the thickness. The extinction length of light is of the order of µm (17). The characteristic thickness of the photoactuators is limited to within an order-of-magnitude of the optical extinction length (18-20). Only slender actuators, at most ~10's of µm in thickness, are capable of presenting any perceivable photomechanical response, typically by bending due to photostrain gradients. Devices with a low bending stiffness (which scales with thickness-cubed) make for weak flexural actuators. Stimuliresponsive muscles often present a force-velocity tradeoff – be it artificial or natural (21). Power amplification via latch-spring mechanisms provides a work-around, be it via an extrinsic latch or an intrinsic geometric latch (22).

Here, we show that photomechanical strain gradients in monolithic geometries that have been geometrically biased via curvatures at rigid boundary conditions, will elicit emergence of hingelike structural articulation and torque-dense actuation. The responsive material, in essence, incorporates a geometric latch. The transverse curved structures are statically stiffer than flat photoactive films. When irradiated, this structure spontaneously bifurcates into a segmented kinematic mechanism composed of two oppositely curved sections connected by a curved crease. Each transversely curved segment retains the magnified bending stiffness and flexure is generated at the crease that is under stretch. The bifurcation is torque-dense and compares favorably against that from conventional actuators and electromechanical systems. The photomechanically-driven morphogenesis is not inherited from explicit patterning of the material geometry (e.g. predefined creases), microstructure (e.g. blueprinted nematic order) or by localizing the optical stimulus. Rather, it emerges in a monolith when the photostrain gradients interplay with the boundary conditions and geometry. This inherent simplicity is useful for the generalizability of the idea across material systems and length-scales to enable photomechanical machines. Beyond the photomechanical actuation demonstrated using ultraviolet (UV) light here, it is possible to utilize the bifurcation of the shell as a broader strategy to upconvert nascent bending into torque-dense actuation.

2. Results and Discussion

Thin sheets that are curved into a shell are stiffer than when they are flat (Figure SI1; (23)). The imposition of a transverse curvature (I/R) in a sheet of length L and thickness t magnifies the bending stiffness in comparison to the flat state by a factor of $\sim \left(\frac{L^2}{Rt}\right)^{\frac{3}{2}}$ (24). Exploiting transverse

curvature is a natural motif that augments the rigidity of human finger nails (25) and feet (26). But mere stiffening of the actuator cannot result in improved performance; if the photomechanical work generated upon irradiation is wasted in to fighting against the higher stiffness, no meaningful actuation will be achieved.

We utilize a glassy, photomechanically responsive azobenzene-functionalized liquid crystalline polymer (ALCP) film (thickness $t = 50 \mu m$; several mm in length and width), characterized by a splayed nematic pattern through the thickness (Figure SI2). Order-disorder transitions in such ALCP result in bending because of the broken symmetry in strain generation that arise from the splayed nematic pattern through the thickness of the film – expansion on the homeotropic surface and contraction along the nematic director on the planar oriented side (27, 28). In addition to the splayed molecular distribution, the light attenuation through the thickness of the film additionally results in a graded strain generation through the thickness of the film (19). When irradiated without being confined, they adopt a spontaneous curvature, bend and remain a developable geometry. Given this, we explored the effect of boundary confinement in samples of length L = 6mm and width W = 10mm that were excised from a $t = 50 \mu m$ film. A 370 μm thick Cu wire was attached using an acrylate glue along the periphery of the sample. When, the wire is straight the sample bends quasistatic as illustrated in Figure SI3. Bending the Cu wire to various radii (R) transforms the flat ALCP film into a transversely curved shell (See Figure SI4 for fabrication steps). The wire imposes a rigid constraint at the periphery. An essential design choice during the fabrication of these shells is to ensure that the molecular director (\bar{n}_o) on the planar side is parallel to L and perpendicular to W (convex side). The opposite, concave surface is homeotropically aligned (\bar{n}_o perpendicular to both L and W). In this study, we restrict ourselves to $L \ll \frac{W^2}{\sqrt{tR}}$, i.e. remaining

within length-scales where the curvature from the boundary confinement persists over the entirety of the sample (29, 30).

Figure 1a illustrates a 3-dimensional profilometric scan of the boundary confined shell (at time t<ton). In Figure 1b, at t=ton the homeotropic side is irradiated with 365nm light with an intensity of 500mW/cm². The equilibrium trans state of the azobenzene is converted to the bent cis form, which results in photomechanical strains that are contractile along \bar{n}_o and tensile orthogonal to it (27). The accumulation of the bent photoisomers disrupts the molecular order and engenders a distortion. In this configuration, the photomechanical strains fight against the rigid boundary constraint and seek to evert the shell. Except, along the corners that are free to respond photomechanically by bending away from the light (cf. t=t_{on}+2s in Figure 1b). In the rest of the sample, the photomechanical strain energy continues to accumulate. At t=t_{on}+2.9s, an energy threshold is crossed, which leads to a bifurcation of the shell along a crease. The shell, which was hitherto of high flexural rigidity snaps to release the accumulated photomechanical work and its tip sweeps through an angle of $\phi \sim \pi/2$. The imaging with a 7-fps camera was inadequate to resolve the transition, suggesting that the actuation likely proceeded at the ms-timescales. The geometry following the actuation is characterized by a crease, which separates the two transversely curved halves (Figure 1c). Parenthetically, we note a correspondence between the structural evolution here and that of a Miura-Ori fold pattern (31). The initial state in the starting curved shell (Figure 1a, inset paper model) can be thought of as a peak fold. Following the actuation in Figure 1c (inset paper model), the doubly curved shell can be thought of as a peak and a valley fold, with the curved crease as a pair of valley folds that maintain compatibility.

The actuation and the nucleation of the curved crease is emergent, dictated by the mechanics. It happens in the absence of either spatially selective patterning of the material's microstructure or selective irradiation. These observations have underlying similarities to structural evolution observed when shells are indented (32) or subjected to a localized mechanical stimulus (e.g. Pogorelov's ridge (33-35)). Here, the optical driving force is sample-wide and unstructured. Given the intensity of UV light used in these experiments, the interplay between photochromic and photothermal effects is likely. We expect these effects to collaborate, although we do not decouple their individual effects. Hinging at the curved crease arises from the photomechanics, without even requiring structural weakening akin to that observed in deformed shells that snap when they are prepatterned to nucleate folding (36).

Using high-speed imaging, the actuation is indeed found to occur at the ms-timescale. Figure 2a illustrates a series of images, spaced 4ms apart. The flexural actuation is accomplished in ~16ms. To resolve the mechanics, a model was developed (see the Materials and Methods). Figure 1b illustrates the computed photomechanical response, where the distribution of the Gaussian curvature is highlighted. This shows how at the end of the actuation cycle, stretching is concentrated along the curved crease, as seen from the side profile view. Overall, the model captures the structural evolution with progressive accumulation of the photostrains (See SI Movie 1 that overlays the experimental observations on the model). Figure 2b illustrates the spatial distribution of the photomechanical strain energy density, which is accumulated in the actuator (front view). The geometry corresponds to that in Figure 1. The strain energy density is initially concentrated along two ridges that form a 'V' shaped region. These are analogous to the stretching ridges identified by Witten (37, 38). This is also revealed in SI Movie 1's inset, which

superimposes the Gaussian curvature onto the undeformed geometry. The strain energy accumulates, until the edge of an instability is reached. Thereafter, ultrafast flexure occurs, during which the strain energy is released to generate torque. The energy drop $(\Delta\psi)$ associated with the actuation (from the models) is shown in Figure 2b, where the non-dimensionalized strain energy of the system is plotted as a function of the accumulated photostrain (along the nematic director). ψ , E, and V are the total strain energy (J), storage modulus ($N.m^{-2}$), and the volume of the system, respectively.

The torque generated at these timescales was calculated from the energy drop $\Delta\psi$ in Figure 2b. A mean torque of τ that leads to flexure over an angle ϕ is generated is determined by $\Delta\psi=|\tau\phi|$ (See SI section Torque Calculation for details). ϕ is measured from the models, which is also verified by the in-situ images of the experiments (cf. Figure 1b). The weight-specific torque density was calculated for a range of geometries (See Figure SI5 and the SI section on Torque-Density) and compared against that for conventional actuators (Figure 2c). Table SI1 illustrates the datapoints used to populate this material property-space.

The ALCP flexural actuator occupies a space that is currently dominated by tethered actuation systems, in particular conventional electromechanical actuators. Feasibility of photoactuators offering torque densities between 1 to 10 N.m/kg and angular velocity ~10² rad/s are an attractive platform in applications that preclude electromechanical systems. These include, manipulation in electromagnetically disruptive environments, applications where electrical power cannot be reliable coupled, as well as microrobotic platforms desiring untethered and remotely controlled

motility. The ability to harness the nascent material response in combination with geometry holds the key to realizing such photoactuation.

The pre-biasing radius (R) imposed at the periphery of the ALCP (Figure 1) is a critical design parameter. Utilizing R = 2.2mm resulted in a curved crease, which is decorated with point-like strain localization (Figure 3a, SI Movie 2). In Figure 3a, the inset shows the Gaussian curvature computed from the models, which highlight the strain localization in developable-cones (d-cones), atop the curved crease. The ease of bending compared to stretching in slender objects such as hanging curtains (32, 39), sheets being forced within confining rings (40) and crumpling leads to d-cones (41). We extract scaling relations between geometry (L, R, t, θ), and the features defining the strain localizations in Figure 3b (L_c , w_c , ϕ). Figures 3c-e illustrate how the geometry of the sample evolves following snap-through. The location of the vertex of the curved crease is found to scale linearly with t/R in Figure 3c across the range of geometries. This figure is populated using data points from the experimental measurements and the simulations. The angle of sweep of the tip of the actuator (ϕ) during the snap-through shows distinct behaviors (Figure 3d) between that corresponding to the integral curved crease versus curved creases with d-cones. We consider the geometry after snap-through to be an isometric transformation that leads to the formation of a mirror-symmetric structure about an osculating plane at the curved crease. As detailed in the SI, the key parameter determining ϕ is $\frac{R\theta^2}{L}$. Given that $\theta = W/R$ (Figure 1a), this can also be written as $\frac{W^2}{RL}$.

The bending (E_b) and the stretching (E_s) energies scale as $E_b \sim Et^3 (\phi/w_c)^2 w_c R_c$ and $E_s \sim Et(\phi w_c^2/R w_c)^2 w_c R_c$. $w_c R_c$ and $\phi w_c^2/R w_c$ represent the area within which the strain energy is

concentrated, and the corresponding Gaussian curvature. Minimizing the total energy $E_r = E_b + E_s$ with respect to w_c , a scaling factor $w_c \sim (tR)^{1/2}$ emerges (32). Figure 3e illustrates the distinctive scaling of W/w_c as a function of $W/(tR)^{1/2}$ for the integral curved crease vs. that with the d-cones. Drawing from Figures 3d and 3e, we utilize $\frac{W^2}{RL}$ and $W/(tR)^{1/2}$ to populate a phase diagram (Figure 3f). Moving diagonally across the phase diagram engenders monotonically increasing torque density, which is indicted for selected points via numbers enclosed in boxes. In this figure, the simulation results for various ranges of initial curvature (0.03 mm⁻¹ \sim 0.6 mm⁻¹), width (6 mm \sim 12 mm), length (3 mm \sim 10 mm) and film thickness (50 μ m \sim 200 μ m) are presented.

Figure 4a illustrates the utilization of flexure to elevate a payload (50 mg), in addition to the weight of the table-like structure (36 mg) (SI Movie 3). ALCP films of dimensions $10\text{mm}(W) \times 6\text{mm}(L) \times 50\mu\text{m}(t)$ are attached to either side of the table. Irradiation with 365nm (500mW/cm^2) from the top drive actuation away from the light and the progressive photostrain accumulation leads to the onset of the creasing instability. The ALCP shells transform into legs and lift a weight 10-times that of the actuators.

Explorations of the photoactuation using the models reveal that the energy accumulation and release is not through the entirety of the curved shell. Figure 2b illustrates that the strain is accumulated in a V-shaped region and is released during the creasing instability. Given this, what is the optimal geometry to maximize the photomechanical work density during the snap-through? We examined a configuration illustrated in Figure 4b, where portions of the actuator near the free edges were progressively excised, and the actuation was modeled. The photostrain required to

drive the sample to the edge of the instability is also shown. We find that $\frac{L_w}{L} = 0.5$ maximizes the work density from the snap-through.

The actuation of a pair of these V-shaped shells was used to fabricate a gripper-like mechanism to grab a cotton-ball using irradiation with 365nm light at 500mW/cm² (SI Movie 4). Here, a single curved shell confined near the middle was utilized and suitable segments were excised with $\frac{L_W}{I}$ 0.5, corresponding to the maximal work-density configuration. Irradiation leads to the tips coming together via flexure to grab a cotton ball. We note the similarity of this light-driven forceps to that of the Origami-based forceps - Oriceps (42) and the Origami 'Chomper' (43). The Oricep has been proposed as a low-profile tool for biomedical applications. Here, the light driven actuation at two curved creases is harnessed to create light-driven forceps, with each crease emulating aspects of the Miura-Ori fold. Figure 4d illustrates a 6 mm × 10 mm × 50 µm photoactuator which is loaded with a load of 10.4mg, which generates moment of inertia of $\sim 1.7 \times 10^{-9} \ kg. \, m^2$. This utilizes a V-shaped element, similar to that utilized in the gripper with $\frac{L_w}{L} = 0.5$. Irradiation results in an ultrafast actuation from the edge of the instability. High speed imaging and motion tracking reveals angular velocity of 73 rad/sec (See SI Movie 5) and a torque density of 3.5 N.m/kg. Using the volume of the curved actuator, a torque per unit volume of 4200 N.m/m³ can be achieved. This experiment is illustrated by the cross sign in Figure 2c to contrast it against conventional actuators. We also illustrate the capability of these curved crease actuators to perform over multiple cycles of actuation, where irradiation to the edge instability was used to trigger snap-through. Then, turning off the light was used to reset the actuator (See Figure SI6).

While, the transverse curvature imposed on the ALCP shell was enforced using rigid constraints, opportunities also emerge for all-optical modulation of the response. That is, light can be used to impose the curvature and subsequently to drive the actuation. This was accomplished by creating a composite structure that is illustrated in Figure 5. First, a lower modulus (~10 MPa) azobenzenefunctionalized liquid crystal polymer (ALCP-LM) was synthesized (See SI for details). A 6mm × $10\text{mm} \times 50\mu\text{m}$ sample, which is characterized by a splayed orientation was excised. To this, the monodomain film of dimension $4\text{mm} \times 10\text{mm} \times 50\mu\text{m}$, cut from stiffer ALCP (modulus ~ 3 GPa) used in the prior experiments (e.g. Figure 1) was attached using an acrylate glue. As illustrated in Figure 5a, the nematic director in the monodomain ALCP film aligned with the glued edge, while the planar side (A) of the ALCP-LM was perpendicular to that edge. Now, irradiating just the monodomain ALCP with 365nm (50mW/cm²) leads to the expected bending towards the actinic light (Figure 5b). The stiffer ALCP deforms the ALCP-LM to impose a curvature upon it. Controlling the irradiation intensity/time is a vehicle for modulating the prebiased curvature imposed on the ALCP-LM. In this illustrative example, a radius of curvature of 6.3mm was imposed on the ALCP-LM. Having imposed this curvature, then irradiating the ALCP-LM on its homeotropic side B with 365nm light (200mW/cm²) drives the formation of the curved crease (Figure 5c and SI Movie 6). This approach offers an all optical route to modulate the response profiles starting with nominally flat composite structures. The ability to build hierarchical structures to exploit the nascent responses is a useful route for building photomechanical actuators that can be both powered and regulated using light.

3. Conclusions

Judicious application of curvatures at the periphery of photoactive liquid crystalline polymers is shown to enable torque-dense actuation with figures-of-merit that compare favorably against conventional electromechanical systems. Slender actuators, which would otherwise bend slowly upon irradiation are shown to generate torque densities approaching 10 N.m/kg at angular velocities $\sim 10^2$ rad/s. An essential feature underpinning such photoactuation is the emergence of a creasing instability, wherein a hitherto developable shell bifurcates into two transversely curved segments. The sections are connected by a curved crease, where the Gaussian curvatures are localized. Such actuation is emergent from the mechanics and is encoded by the geometry. The phase-space characterizing the actuation is derived as a function of the prebiasing curvature and dimensions of the photoactive film. Two distinct actuation modalities emerge: one, characterized by the nucleation of a curved crease; and the other, characterized by the decoration of the curved crease by point-like strain concentrations. The photoactuation is harnessed in prototypical applications, including lifters, grabbers and levers capable of multiple actuation cycles. The overall framework is also shown to open a pathway for regulating the torque dense actuation using composite architectures, where a stiffer photoactive polymer is used to controllably impose transverse curvature onto a film, which then generates the torque-dense photoactuation upon irradiation. The actuation profiles of photoactuators can be modulated using light itself.

4. Experimental Methods

Synthesis of Splayed Azobenzene-Functionalized Liquid Crystalline Polymers.

The ALCP films were formulated by mixing 91 wt% (Merck's RMM34C reactive mesogen mixture), 8 wt% 4,4'(-di(8(acryloxy)octylloxy)azobenzene) (8C azo), and 1 wt% photoinitator Irgacure (I-784). The azobenzene crosslinker was synthesized using the procedure in Ref.(17). A polymerization cell with a 50µm gap was fabricated using two glass slides with one surface enforcing planar alignment and the other driving homeotropic alignment. The planar alignment

was achieved by rubbing a spin-coated polyimide (Elvamide Dupont 8023R) layer. The homeotropic state on the other glass was induced using Nissan Chemical SE5661. The gap was set using silica beads of the respective diameter. After fabricating the cell, the monomer mixture was heated to 120 °C for homogeneous mixing in an isotropic state and drawn the polymerization cell via capillarity. The molten mixture is subsequently cooled to 65 °C for nematic states and photopolymerized by Edmund MI-150 high-intensity illuminator equipped with a cut off filter ($\lambda \ge 420$ nm, 35 mW/cm²) for 30 min. Curved shell actuators were fabricated via the steps illustrated in the SI. Figure SI4 illustrates the fabrication steps. The monodomain ALCP in Figure 5 was fabricated using a similar approach. Except that both the glass slides were coated with Elvamide and rubbed after which they were glued together using spacers to create a polymerization cell.

Experimental Setup. The optical setup was built using an OmniCure AC450 Curing LED lamp systems (365nm). A tweezer held the curved sample in front of the UV source such that the concave side (homeotropic) was irradiated. 365nm unpolarized UV light of 500 mW/cm² intensity was used. Two Mighty Scope 1.3M USB Digital Microscope (200x magnification with 7 frames/s) were used for recording the experiments from the side and the bottom of the samples. The recorded data was analyzed using an in-house-developed MATLAB code. The high-speed imaging was done using PHANTOM V2511 High Speed Video Camera (1000 fps). The data from high-speed camera was analyzed using motion analysis software TEMA 4.2. 3D scanning of the curved actuators was done using Wide-area 3D Measurement System VR–3000 Series. Prior to 3D scanning, the samples were sprayed with Helling 3D Laser Scanning Spray to be opaque.

Continuum Model. We use the strain energy density function proposed in Ref.(44) for modeling the behavior of the glassy liquid crystal polymers. The model assumes an isotropic Neo-Hookean energy density function, $W(\mathbf{F}, \mathbf{n}) = \frac{\mu}{2} trace(\mathbf{F}^{eT} \mathbf{F}^{e})$, to define the elastomeric behavior of matrix. The model is assumed to be isotropic to enable a computationally frugal exploration of a range of geometries. However, accounting for the mechanical anisotropy of ALCP will lead to further gains in the fidelity of the models. $F^e = g^{-1}F$ is the elastic deformation gradient written in terms of the total deformation gradient, ${\pmb F}$, and the spontaneous deformation tensor, ${\pmb g}$. Tensor ${\pmb g}=a^{1/3}{\pmb n}\otimes{\pmb n}$ + $a^{-1/6}(I - n \otimes n)$, represents the effect of stimuli by deforming with magnitude $a^{1/3}$ along the nematic director and $a^{-1/6}$ in the plane normal to the director. The parameter a represents the spontaneous deformation of the ALCP and a = 1 when there are no stimuli and the structure is at the relaxed state. When the system is irradiated from the relaxed state a becomes less than 1. To capture the mechanical snapping of the actuator in our quasi-static simulations, the value of a is decreased by 0.001 in each step. n is the vector field defining the current distribution of nematics in the 3D structure of the ALCP. In the glassy systems the deformation of n is not independent from its polymeric network, hence $n = Fn_0/|Fn_0|$. n_0 is the vector field representing the initial distribution of nematics. The energy density function is $W(\mathbf{F}, \mathbf{n_0}) = \frac{\mu a^{\frac{1}{3}}}{2} \left(trace(\mathbf{C}) - \frac{\mu a^{\frac{1}{3}}}{2} \right)$ $(1-a^{-1})\frac{|cn_0|^2}{n_0.cn_0} - \mu \ln(J) + \frac{\kappa}{2} \ln(J)^2$. μ , κ , and J are the material's shear modulus, bulk modulus, and the Jacobian of \mathbf{F} , respectively. The last two terms are added to the energy density function as volumetric penalty terms to approximately enforce incompressibility (45). We choose the reference configuration of the system to be its natural state (i.e. stress-free state). Tensor C = C $\mathbf{F}^T \mathbf{F}$ is the right Cauchy-Green tensor. The values for μ , κ are obtained by relating the Young's modulus and Poisson's ratio of the polymer to its shear and bulk moduli. Young's modulus (E) of the material is assumed to be equal to the storage modulus extracted from the Dynamic Mechanical Analysis (DMA) test and the Poisson's ratio (ν) is taken to be 0.45. Using equations $\mu = E/2(1 + \nu)$ and $\kappa = E/3(1 - 2\nu)$, the values 0.35 GPa and 3.3 GPa are calculated for the shear and bulk moduli, respectively.

Modeling and Simulation Results. Nonlinear finite element modeling was performed using commercial solver, COMSOL Multiphysics (Version 5.4). We model the liquid crystal polymer as a full 3D structure. The Curvilinear Coordinates module is used for solving the vector field that represents the initial nematic alignments in the shells, n_0 . The Solid Mechanics module is used for defining the material properties, governing equations, and the boundary conditions. Iterative Newton's method with variable damping factor is used for solving the stationary model. In order to improve the convergence of the nonlinear problem load ramping is implemented using the Auxiliary Sweep extension. The ramping in performed on the parameter a. The results were analyzed with in-house-developed MATLAB code, MATLAB R2019a.

Acknowledgements

Support from the National Science Foundation 1635926 (Pitt) and 1635407 (CMU) are gratefully acknowledged. M.R.S. and K.D. also acknowledge support from the Office of Naval Research (N00014-18-1-2856, N00014-18-1-2528).

References

- 1. A. H. Gelebart *et al.*, Making waves in a photoactive polymer film. *Nature* **546**, 632 (2017).
- J. J. Wie, M. R. Shankar, T. J. White, Photomotility of polymers. *Nature communications* 7, 13260 (2016).
- 3. C. Ahn, X. Liang, S. Cai, Bioinspired Design of Light-Powered Crawling, Squeezing, and Jumping Untethered Soft Robot. *Advanced Materials Technologies*, 1900185 (2019).
- 4. J.-a. Lv *et al.*, Photocontrol of fluid slugs in liquid crystal polymer microactuators.

 Nature **537**, 179 (2016).
- 5. G. Vantomme, A. Gelebart, D. Broer, E. Meijer, A four-blade light-driven plastic mill based on hydrazone liquid-crystal networks. *Tetrahedron* **73**, 4963-4967 (2017).
- 6. F. Lancia, A. Ryabchun, N. Katsonis, Life-like motion driven by artificial molecular machines. *Nature Reviews Chemistry*, 1-16 (2019).
- 7. T. Hiscock, M. Warner, P. Palffy-Muhoray, Solar to electrical conversion via liquid crystal elastomers. *Journal of Applied Physics* **109**, 104506 (2011).
- 8. Y. Yu, M. Nakano, T. Ikeda, Photomechanics: directed bending of a polymer film by light. *Nature* **425**, 145 (2003).
- 9. H. Finkelmann, E. Nishikawa, G. Pereira, M. Warner, A new opto-mechanical effect in solids. *Physical Review Letters* **87**, 015501 (2001).
- 10. B. A. Kowalski, C. Mostajeran, N. P. Godman, M. Warner, T. J. White, Curvature by design and on demand in liquid crystal elastomers. *Physical Review E* **97**, 012504 (2018).
- 11. M. Hendrikx *et al.*, Re-and Preconfigurable Multistable Visible Light Responsive Surface Topographies. *Small* **14**, 1803274 (2018).

- 12. M. Hendrikx, A. Schenning, D. Broer, Patterned oscillating topographical changes in photoresponsive polymer coatings. *Soft Matter* **13**, 4321-4327 (2017).
- 13. T. J. White, D. J. Broer, Programmable and adaptive mechanics with liquid crystal polymer networks and elastomers. *Nature materials* **14**, 1087 (2015).
- 14. S. Iamsaard *et al.*, Conversion of light into macroscopic helical motion. *Nature chemistry* **6**, 229 (2014).
- 15. S. Palagi *et al.*, Structured light enables biomimetic swimming and versatile locomotion of photoresponsive soft microrobots. *Nature materials* **15**, 647-653 (2016).
- 16. F. Cheng, R. Yin, Y. Zhang, C.-C. Yen, Y. Yu, Fully plastic microrobots which manipulate objects using only visible light. *Soft Matter* **6**, 3447-3449 (2010).
- 17. A. Skandani, J. A. Clement, S. Tristram-Nagle, M. R. Shankar, Aliphatic flexible spacer length controls photomechanical response in compact, ordered liquid crystalline polymer networks. *Polymer* **133**, 30-39 (2017).
- 18. M. Warner, C. Modes, D. Corbett, Curvature in nematic elastica responding to light and heat. *Proceedings of the Royal Society A: Mathematical, Physical and Engineering Sciences* **466**, 2975-2989 (2010).
- 19. C. L. van Oosten *et al.*, Bending dynamics and directionality reversal in liquid crystal network photoactuators. *Macromolecules* **41**, 8592-8596 (2008).
- D. Corbett, C. Van Oosten, M. Warner, Nonlinear dynamics of optical absorption of intense beams. *Physical Review A* 78, 013823 (2008).
- 21. L. C. Rome, S. L. Lindstedt, The quest for speed: muscles built for high-frequency contractions. *Physiology* **13**, 261-268 (1998).

- 22. M. Ilton *et al.*, The principles of cascading power limits in small, fast biological and engineered systems. *Science* **360** (2018).
- 23. M. Taffetani, F. Box, A. Neveu, D. Vella, Limitations of curvature-induced rigidity: How a curved strip buckles under gravity. *EPL (Europhysics Letters)* **127**, 14001 (2019).
- 24. M. Venkadesan *et al.*, Stiffness of the human foot and evolution of the transverse arch.

 Nature **579**, 97-100 (2020).
- 25. H. P. Baden, The physical properties of nail. *Journal of investigative dermatology* **55**, 115-122 (1970).
- 26. N. B. Holowka, D. E. Lieberman, Rethinking the evolution of the human foot: insights from experimental research. *Journal of Experimental Biology* **221**, jeb174425 (2018).
- 27. C. Van Oosten, K. Harris, C. Bastiaansen, D. Broer, Glassy photomechanical liquid-crystal network actuators for microscale devices. *The European Physical Journal E* 23, 329-336 (2007).
- 28. G. N. Mol, K. D. Harris, C. W. Bastiaansen, D. J. Broer, Thermo-mechanical responses of liquid-crystal networks with a splayed molecular organization. *Advanced Functional Materials* **15**, 1155-1159 (2005).
- 29. T. Barois, L. Tadrist, C. Quilliet, Y. Forterre, How a curved elastic strip opens. *Physical review letters* **113**, 214301 (2014).
- 30. A. E. Lobkovsky, T. Witten, Properties of ridges in elastic membranes. *Physical Review E* **55**, 1577 (1997).
- 31. M. Schenk, S. D. Guest, Geometry of Miura-folded metamaterials. *Proceedings of the National Academy of Sciences* **110**, 3276-3281 (2013).

- 32. M. Das, A. Vaziri, A. Kudrolli, L. Mahadevan, Curvature condensation and bifurcation in an elastic shell. *Physical review letters* **98**, 014301 (2007).
- 33. A. V. e. Pogorelov, *Bendings of surfaces and stability of shells* (American Mathematical Soc., 1988), vol. 72.
- 34. M. Gomez, D. E. Moulton, D. Vella, The shallow shell approach to Pogorelov's problem and the breakdown of 'mirror buckling'. *Proceedings of the Royal Society A:*Mathematical, Physical and Engineering Sciences **472**, 20150732 (2016).
- 35. L. Pauchard, S. Rica, Contact and compression of elastic spherical shells: the physics of a 'ping-pong'ball. *Philosophical Magazine B* **78**, 225-233 (1998).
- 36. N. P. Bende *et al.*, Geometrically controlled snapping transitions in shells with curved creases. *Proceedings of the National Academy of Sciences* **112**, 11175-11180 (2015).
- 37. A. Lobkovsky, S. Gentges, H. Li, D. Morse, T. A. Witten, Scaling properties of stretching ridges in a crumpled elastic sheet. *Science* **270**, 1482-1485 (1995).
- 38. J. Fuentealba, O. Albarrán, E. Hamm, E. Cerda, Transition from isometric to stretching ridges in thin elastic films. *Physical Review E* **91**, 032407 (2015).
- 39. E. Cerda, L. Mahadevan, J. M. Pasini, The elements of draping. *Proceedings of the National Academy of Sciences* **101**, 1806-1810 (2004).
- 40. E. Cerda, L. Mahadevan, Confined developable elastic surfaces: cylinders, cones and the Elastica. *Proceedings of the Royal Society A: Mathematical, Physical and Engineering Sciences* **461**, 671-700 (2005).
- 41. T. A. Witten, Stress focusing in elastic sheets. *Reviews of Modern Physics* **79**, 643 (2007).

- 42. B. J. Edmondson *et al.* (2013) Oriceps: Origami-inspired forceps. in *ASME 2013*conference on smart materials, adaptive structures and intelligent systems (American Society of Mechanical Engineers Digital Collection).
- 43. J. Shafer, *Origami Ooh La La!: Action Origami for Performance and Play* (CreateSpace, 2010).
- 44. A. DeSimone, L. Teresi, Elastic energies for nematic elastomers. *The European Physical Journal E* **29**, 191-204 (2009).
- 45. A. G. Holzapfel, Nonlinear solid mechanics II. (2000).

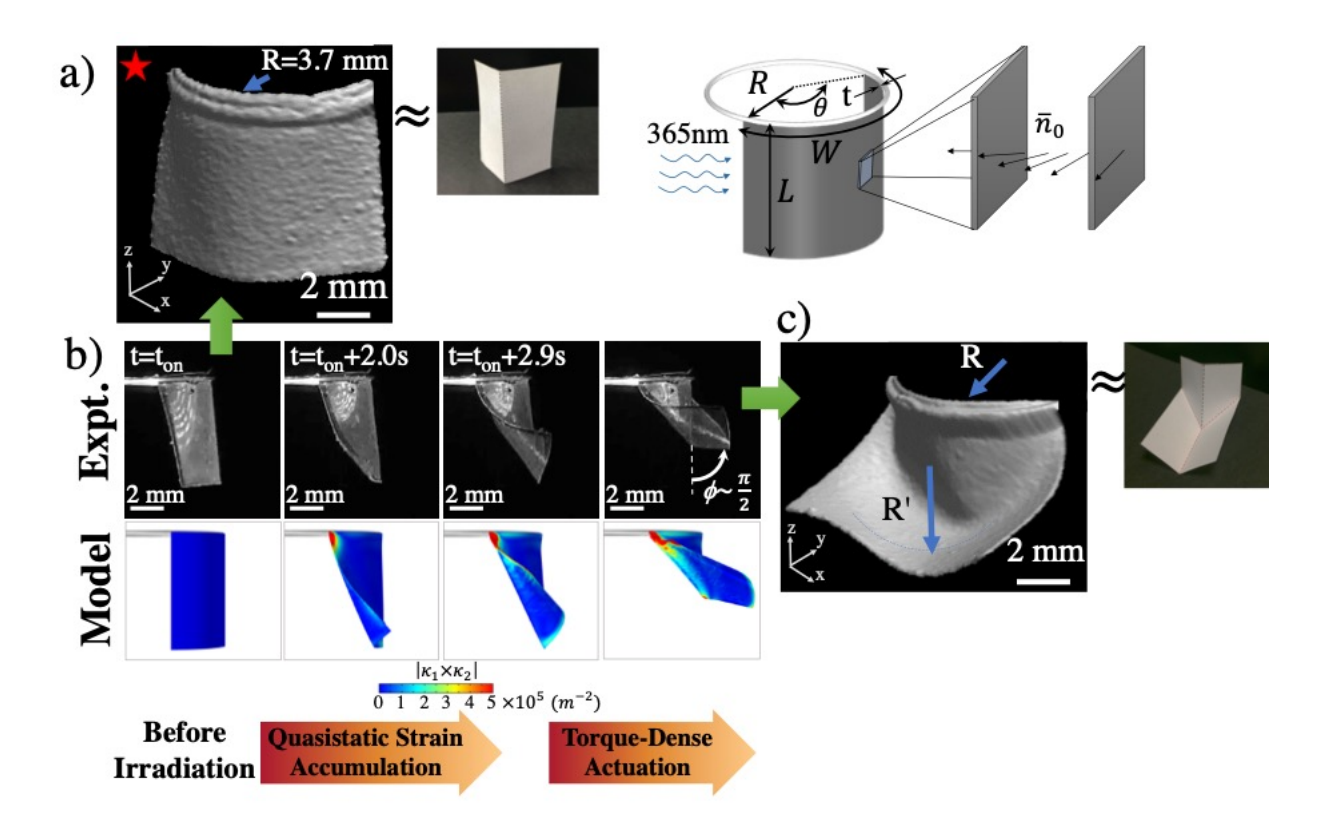


Figure 1: a) Initial geometry of a curved shell fabricated from an ALCP sample 10mm(W) x 6mm(L) x $50\mu\text{m}(t)$ that is irradiated with 365 nm light at an intensity of 500mW/cm^2 . The curvature (R = 3.7 mm) is imposed using rigid confinement from a curved copper wire that is attached to the sample along its periphery. The molecular orientation through the thickness is illustrated; light impinges on the homeotropic surface. The photomechanical response of this geometry is marked with a red * and is also identified in the phase diagram in Figure 3f. b) Side view of the structural evolution in time steps is illustrated; experiment (top row) and simulation (bottom row). The snapshots from the simulation demonstrates the distribution of the Gaussian curvature that develops in the sample as a result of the photoresponse. c) 3D scanning result of the doubly curved configuration that develops at the end of the actuation cycle is illustrated. A curved crease separates the sample into two oppositely curved halves with radius of R = 3.7 mm and R' = 5.41 mm. This structure loosely mimics a Miura-Ori fold pattern, which evolves from

the prior shell in a), which is analogous to a peak fold. SI Movie 1 illustrates the progressive evolution of the structure as a function of time.

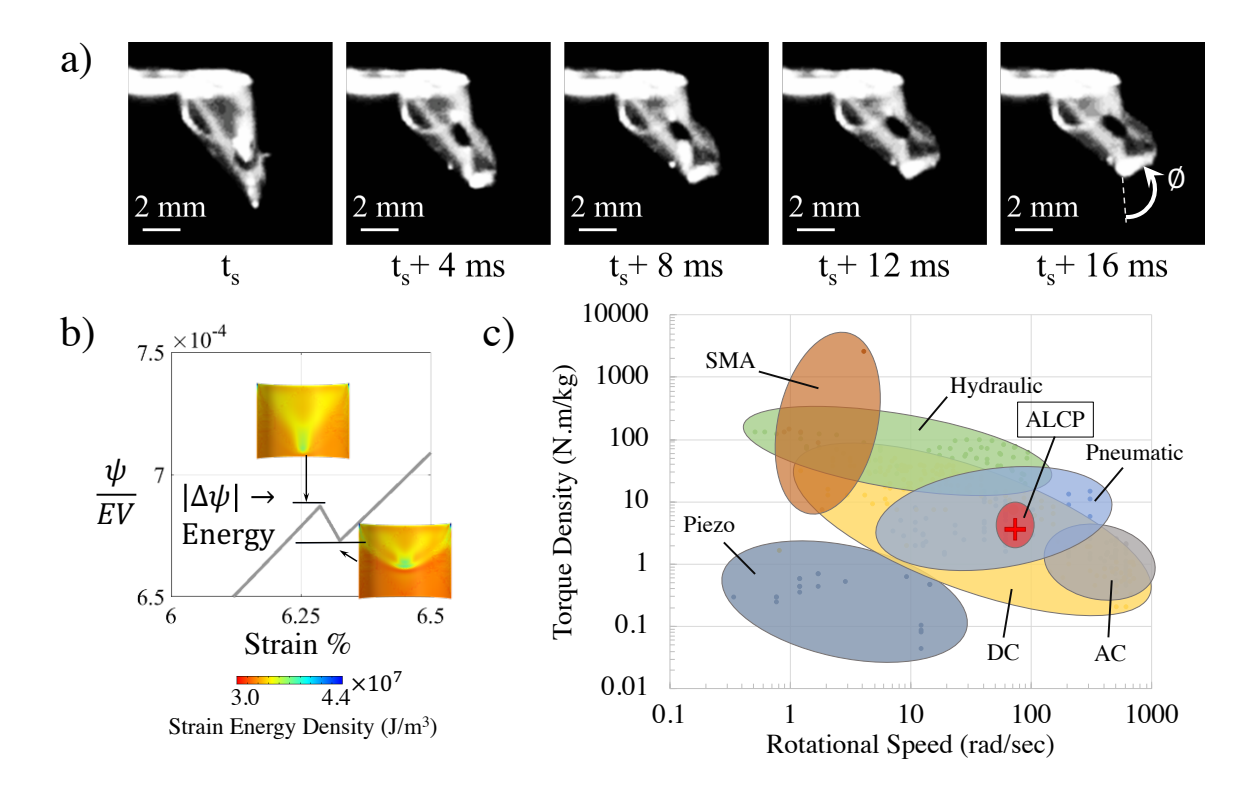


Figure 2: a) Snap-through during the curved crease formation as revealed by 1000fps imaging. b) The evolution of the strain energy of the sample in Figure 1 is illustrated as a function of the contractile photostrain that is accumulated along the nematic director. ψ , E, and V are the total strain energy (J), storage modulus ($N.m^{-2}$) and the volume of the system. At a strain of $\varepsilon_p \sim 6.3\%$, part of the energy is released. E and V are the elastic modulus and the volume of the active material. A curved crease is generated during the flexural actuation. c) The torque density and the rotational speed of the ALCP actuators is compared against other tethered systems. The ability to scale the torque densities in the range of 1-10Nm/kg is illustrated in Figure SI5.

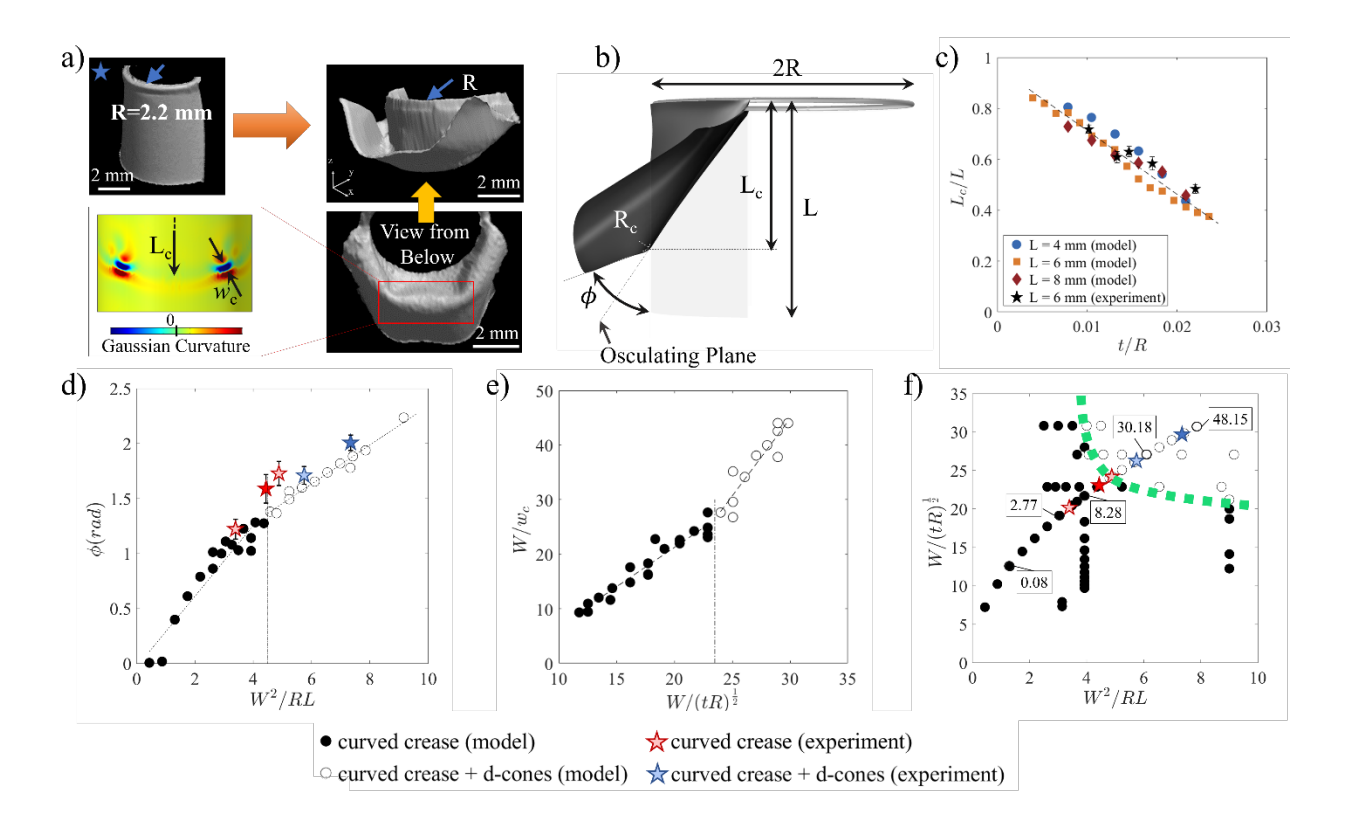


Figure 3: a) 3D scan image of a 6 mm × 10 mm × 50 μ m sample prebiased to a curvature of R=2.2mm. Two point-like strain localizations are observed after snap-through, which occurs at a photostrain of $\varepsilon_p \sim 9.64\%$. The photomechanical response of this geometry is marked with a dark blue * and is also identified in the phase diagram in f. See SI Movie 2 that overlays experimental observation of the geometry against that from the model. b) Schematic of the photomechanically deformed shell illustrating the geometric parameters. The relationship between the geometry and the resulting actuation responses are extracted from analytic and computational models. These include, c) simulations and measurements of the L_c/L as a function of t/R, d) ϕ as a function of W^2/RL and e) W/w_c as a function of $W/(tR)^{1/2}$. f) Using the scaling behavior observed in (d-e) a phase diagram was delineated. Two distinct regions separated by a transition zone shown with a green dashed line emerge. One corresponding to the creation of a curved crease, while another

characterized by a curved crease that is decorated with d-cones. The numbers in the boxes illustrate the torque densities (N.m/kg) that can be generated during the snap-through. The dark red * corresponds to the structure shown in Fig. 1a, and the dark blue * corresponds to the structure in Fig. 3a.

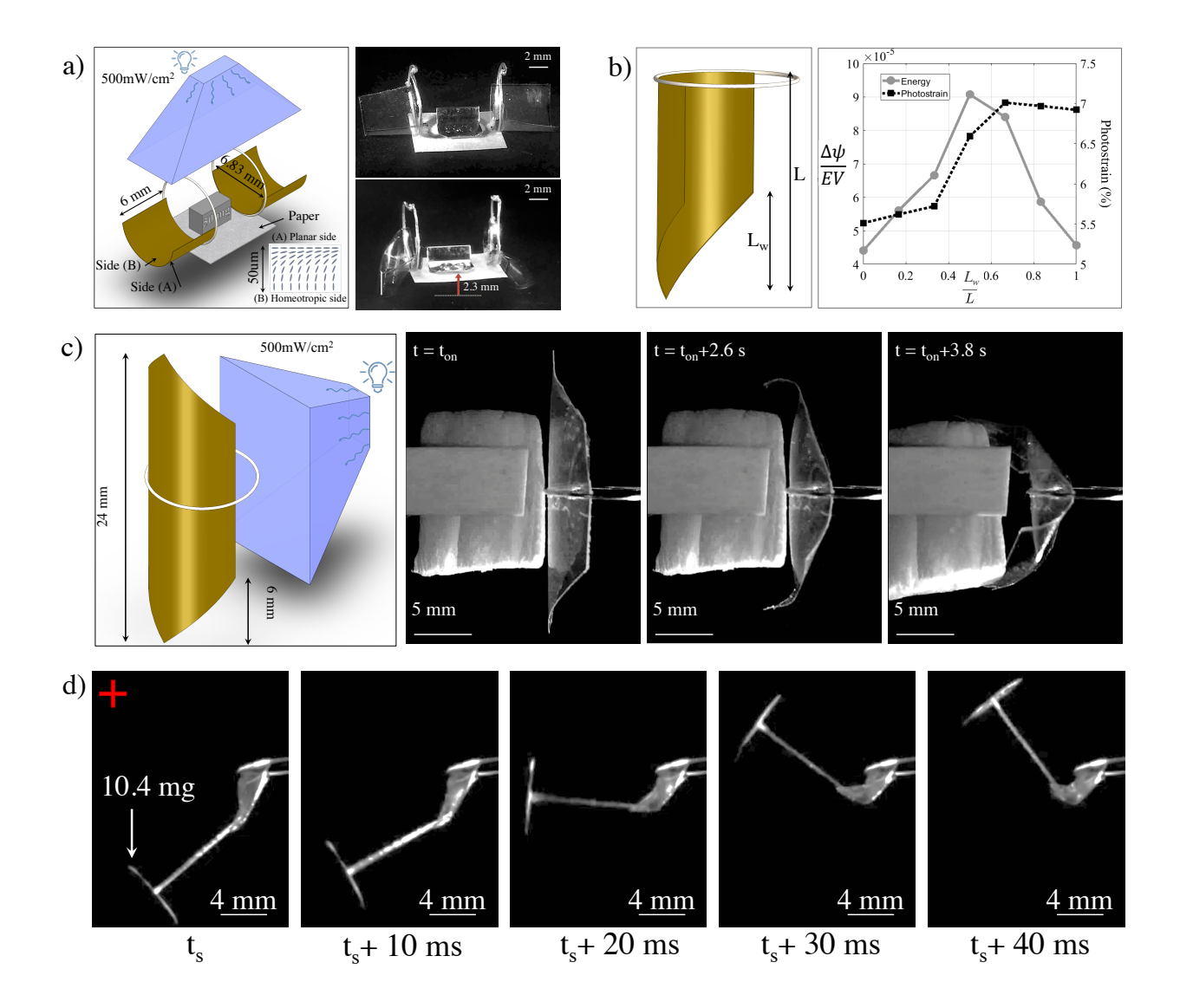


Figure 4: a) Harnessing the flexural actuation from snap-through in a vertical lifter. A prebiased curvature on the splayed ALCP legs is imposed using metal rings that are also attached to a piece of paper that is used as a table to carry a weight. Irradiation with 365nm light at 500 mW/cm² drives the lifting of a weight of 50 mg + 36 mg (weight on the paper + paper + metal rings). See SI Movie 3. b) $L_w/L=0.5$ is revealed as the geometry that maximizes the work density generated from the snap-through. The photostrains required to drive the sample to the edge of instability are illustrated as a function of the geometry. c) A structure composed of a pair of work dense ALCP

actuators emulates a gripper mechanism using irradiation with 365nm (500mW/cm²). In this structure, the optimized geometry from (b) with $L_w/L=0.5$ is used. See SI Movie 4. d) The actuator that was harnessed for the grippers was characterized for its torque generation against an applied load. This configuration also corresponds to the data point marked with a red + in Figure 2c. Here, a 10.4 mg weight is glued to the curved 3.6 mg splayed nematic ALCP film of dimension 6mm×10mm×50 μ m and is irradiated with UV light of intensity 500 mW/cm². The motion is analyzed using the motion analysis software, TEMA. The maximum angular velocity of 73 rad/sec and torque density of 3.5 N.m/kg is measured. See SI Movie 5.

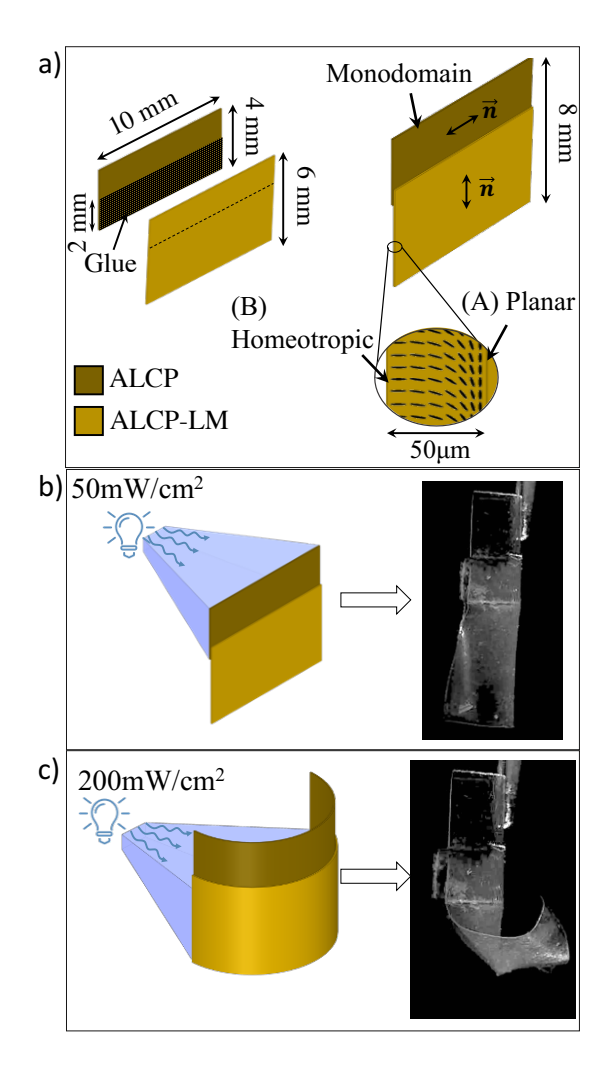


Figure 5: The geometry of the optically powered curved crease actuators can be modulated using light itself to control the actuation profiles. a) Monodomain ALCP sample (darker part at the top) is used to bend and prebias the transverse curvature of a splayed, azobenzene-functionalized liquid crystal polymer of a lower modulus (ALCP-LM). The films are glued together along their longer edge. The homeotropic side of the splayed ALCP-LM faces the 365nm light. b) The first step of irradiation (50 mW/cm²) is limited to the upper piece which tunes the imposed curvature on the entire structure. c) The second step of irradiation (200 mW/cm²) is on the softer ALCP-LM zone, which leads to the curved-crease formation.

Table of Contents

Polymeric actuators that are remotely powered using light are shown to demonstrate torque-densities that are comparable to that obtained from electromechanical systems. Photomechanical actuation occurs at ms-time scales and generates torque-densities that are scalable from 1-10Nm/kg. Illustrative examples implement this actuation in lifters, grabbers and levers that can be repetitively actuated and controlled exclusively using light.

